Materials Today: Proceedings 39 (2021) 1132–1140

Contents lists available at ScienceDirect

Materials Today: Proceedings

journal homepage: www.elsevier.com/locate/matpr

High thermally stable hybrid materials based on amorphous porous silicon nanoparticles and imidazolium-based ionic liquids: Structural and chemical analysis

Mohamed R. Tchalala [a,*], Jehad K. El-Demellawi [a], Parvathalu Kalakonda [a], Sahraoui Chaieb [b,c]

[a] Division of Physical Sciences and Engineering, King Abdullah University of Science and Technology, Thuwal 23955-6900, Saudi Arabia
[b] Biological and Environmental Sciences and Engineering (BESE) Division, King Abdullah University of Science and Technology, Thuwal 23955-6900, Saudi Arabia
[c] Lawrence Berkeley National Laboratory, Chemical Sciences Division, 1 Cyclotron Road, Mailstop 6R-2100, Berkeley, CA 94720, United States

ARTICLE INFO

Article history:
Received 2 December 2019
Accepted 26 March 2020
Available online 28 April 2020

Keywords:
Ionic liquids (ILs)
Amorphous porous silicon
Nanoparticles (ap-Si NPs)
(ILs)-(ap-Si NPs) Nanocomposites
Thermogravimetric analysi
Raman shifts

ABSTRACT

Compared to conventional solvents, ionic liquids (ILs) are highly recognized for their ability to enhance the dispersion of nanoparticles (NPs). However, the thermal stability of the ILs-based nanocomposites is a vital parameter for their processing applications. Here, we scrutinized the thermal stability of a series of different imidazolium ion-based ILs before and after incorporating amorphous porous silicon (ap-Si) NPs. The results show that regardless of the obtained quality dispersion, the thermal stability of the host ILs was never regressed. The combination of ap-Si NPs and bmim-SCN (1-buthyl-3-methyl imidazolium thiocyanate) induced highly dispersed framework with an enhanced thermal stability (~15 °C shift to higher temperature). Likewise, the emim-BF_4 (1-ethyl-3-methylimidazolium tetrafluoroborate) coated the ap-Si NPs forming a very stable dispersion along with a good thermal stability (~8 °C shift). On the other hand, the thermal stability of bmim-Ac (1-buthyl-3-methylimidazolium acetate) was not affected owing to the high viscosity of bmim-Ac that limited the dispersion of ap-Si NPs at room temperature. Throughout our study, we explored the intermolecular interactions using SEM, TEM, Raman spectroscopy and XRD. We probed the thermal stability of the fabricated dispersions using TGA, and DSC as part of characterization methodology.

Selection and peer-review under responsibility of the scientific committee ofthe5thEuro-Mediterranean Conference on Materials and Renewable Energies.

1. Introduction

Over the past decade, an enormous number of studies have been devoted to the synthesis of architectural inorganic NPs in a stable nanocomposite for multi-tasking nanomaterials as a new thrust area of research [1]. However, a homogeneous distribution of inorganic NPs in the host solvents is not always obtained due to the poor compatibility of inorganic NPs in aqueous and non-aqueous solvents. Moreover, the ability of solvents to preserve a stabilized dispersions of NPs has proven to be problematic [2,3]. For any host medium, dispersion of NPs is an important state of matter for fundamental research. However, maintaining a well-dispersed stable state is very challenging for various NPs. The extreme low solubility of many NPs reduces the quality of their dispersions [4,5]. Furthermore, the characteristics of colloidal systems are often hampered by the spontaneous tendency of NPs to aggregate [6], irrespective of the type of NPs employed to decrease aggregation. Because of their high surface energy which dominates their properties, NPs; especially small ones, need to be stabilized to avoid their agglomeration [6].

In this regard, several processing methods have been used to obtain a thermodynamically stable dispersion of NPs in solutions including the use of surfactants, polymers, and dendrimers, to prevent the self-aggregation of NPs [7]. When used, surface capping ligands or polymers form a protective layer on the surface of the NP which provides steric coverage, yielding products with sufficient stability against aggregation. This surface coverage induces a partial deactivation of surface activities, leading to a set of new physicochemical properties compared to single-component particles [8,9]. Ionic stabilizers, in particular, are the best stabilizers

* Corresponding author.
E-mail address: mohamed.tchalala@kaust.edu.sa (M.R. Tchalala).

https://doi.org/10.1016/j.matpr.2020.03.706
2214-7853/
Selection and peer-review under responsibility of the scientific committee ofthe5thEuro-Mediterranean Conference on Materials and Renewable Energies.

for NPs. They adsorb strongly enough and meet the conceptions of steric and electrostatic stabilization simultaneously [7,8].

In this context, ILs, a class of organic salts that are entirely composed of cationic organic species and anionic inorganic or organic species, have garnered a lot of interest as strong stabilizing agents for NPs. They allow for having stable dispersions without the need of additional stabilizers [10]. ILs are multipurpose materials that retain distinctive unique properties such as wide liquid range, low volatility, high ionic conductivities and wide electrochemical window and high thermal stability [11–16].

They are also considered as promising green solvents because of being environmentally benign with remarkably low toxicity. They are now widely recognized as suitable catalysts and solvents for synthetic chemical reactions, liquid-liquid extraction, gas separation, and recycling [10,14]. ILs can be especially "designed" for the stabilization of NPs. To date, several stable dispersions of NPs in ILs have been reported based on a large variety of different kinds of NPs and ILs. Extensive recent studies have been reported on the utilization of ILs, especially those based on imidazolium cation, for the stabilization of colloids by varying the cation-anion combination [10,13,15,16]. The dispersion of NPs in ILs allows for the formulation of novel ILs-based nanocomposite materials that combine the properties and functionality of the NPs with the characteristics of ILs. However, the effect of dispersing NPs on the thermal behavior of the host ILs was not thoroughly investigated. In general, studying the thermal behavior of ILs is vital for designing new applications in catalysis and energy storage based on ILs [17].

In this work, we studied the dispersion quality of amorphous porous silicon (ap-Si) NPs in imidazolium-based ILs and their; ap-Si NPs, effect on the thermal behavior of the host ILs. Like numerous other semiconductor NPs, ap-Si NPs exhibit a net electrodynamic attraction and experience quantum confinement effects leading to exciting properties [13,18–21]. Recently it was shown that the dispersion of ap-Si NPs in imidazolium-based ILs has widened the electrochemical window of the incorporated ILs and enhanced the electrical conductivity [15]. The thermal stability of those dispersions, however, remains unexplored. Moreover, despite the versatile applications of IL-NPs nanocomposites, the dispersion mechanism for NPs in ILs remains still unclear. For this purpose, we have investigated in-depth the dispersion mechanism of ap-Si NPs in ILs, where the ILs-NPs interactions are highly favorable. We also investigated how the properties of these new nanocomposite formulations had affected the thermal stability of the ILs.

2. Experimental section

2.1. Materials synthesis

Amorphous porous silicon nanoparticles (ap-Si NPs) were prepared using a developed stain etching method.[22,23] ap-Si NPs suspensions were fabricated through etching (1 0 0) single crystal silicon wafers (p-type boron doped, Addison Electronics). The wafers were laser-cut into rectangular strips. The silicon strips were submerged in an etching bath composed of 4.71 g anhydrous iron(III) chloride (98%, Alfa Aesar) dissolved in a mixture of 18 ml of hydrochloric acid (32%, Fischer Scientific) and 42 ml of hydrofluoric acid (49%, Fluka). The strips were left in the etching bath for 13 h, after which their surface became matte black. We cleaned the etched strips by rinsing them with deionized water (Millipore) followed by absolute ethanol (Sigma Aldrich). We dried the etched strips under a nitrogen stream. Afterward, we submerged the etched strips in toluene (Chromasolove grade, Fischer Sci.), and sonicated them for 45 min using a VWR Ultrasonic Cleaner sonicating bath. We then used a LabConco RapidVap vacuum evaporation system to evaporate the ap-Si NPs solutions.

Product yields were estimated to be approximately 0.4 mg of ap-Si NPs per cm^2 of the etched silicon. The quantum yield of the nanostructures dispersed in toluene was found to be around 50%. The synthesized particles were found to be hundreds of nanometers in size.

We suspended the dried ap-Si NPs in three different ionic liquid formulations (99% purity, Sigma-Aldrich). Each glass vial contained 0.036 g of ap-Si NPs in 3 ml of ILs, i.e., 1-butyl-3-methylimidazolium thiocyanate (bmim-SCN), 1-ethyl-3-methylimidazolium tetrafluoborate (emim-BF_4) and 1-butyl-3-methylimidazolium acetate (bmim-Ac), respectively.

2.2. Instrumentation

Dispersions of ap-Si NPs-containing ILs were handled in an argon-filled MB GB 2202-C acrylic glove box (MBraun). We scanned our samples using a Horiba X-Ray fluorescence analyzer (XRF). The working power was 30 kV. The preset time was 100 s with current value of 0.05 mA and 3XGT:1.2 mm processed under full vacuum mode. Scanning electron microscopy (SEM) images were taken using a Nova NanoSEM 450 scanning electron microscope (FEI) working in the secondary electrons mode at a voltage of 2 kV and a resolution of 2 nm. High-resolution transmission electron microscopy (HRTEM) micrographs were taken using an FEI Titan Krios CT-TEM at an operating voltage of 120 kV. The porosity measurements were conducted at −196 °C with an ASAP 2420 (Micromeritics) 6 ports volumetric analyzer.

Raman spectra were acquired by Horiba Jobin Yvon LabRaman HR 800 with a5sX10 integration time. A 532 nm solid-state laser was used as an excitation source. The typical laser power at the sample position was ~4 mW. To avoid the heating effect, a new innovative DuoScan technology was adopted, which scans the laser beam across a 20 × 20 μm^2 area with the help of a combination of scanning mirrors. Powder X-ray diffraction (XRD) was performed on a Bruker D8-Advance diffractometer using Cu-Kα radiation (1.54 Å) with LynxEye 1-D detector. The working power was 40 kV/40 mA with divergence slit of 0.50/1 mm. The stability of ap-Si NPs in different ILs was further investigated by thermogravimetric (TGA) and differential scanning calorimetry (DSC) analyses using STA 449 F1 (Netzsch) analyzer at a temperature range of 30–500 °C. The heating rate was 10 °C/min under a nitrogen flow.

3. Results and discussion

We were able to produce large amounts of amorphous porous silicon using electrolytic stain etching, which was proven to be a fast, simple and cost-effective synthesis route [22,23]. The XRF spectrum of our samples Fig. 1 showed that silicon was the most dominating element (~99 at.%) with some traces of iron (0.69 at. %). The iron is mostly from the iron salt used during etching.

The SEM micrographs revealed a high-density of the stain-etched ap-Si NPs Fig. 2a. The magnified image clearly shows the relatively round shapes of the ap-Si NPs with a size distribution in the range of 50–400 nm. Unevenly distributed agglomerated spherical particles were also present [23]. The HRTEM micrograph, depicted in Fig. 2b illustrates the shapes, the size variation and the porous structure of ap-Si NPs as observed in the prepared suspensions. Most of the NPs were composed of a lacey network of nanometer scale bridges which connect larger aggregates of different sizes dispersed in toluene solution. Obviously, the NPs with larger size grow at the cost of smaller one due to higher surface free energy. Furthermore, the Brunauer-Emmett-Teller (BET) porosity measurements see Fig. 2c. Confirmed the highly porous structure of ap-Si NPs observed in the TEM. The fabricated NPs have an average surface area of 135 m^2/g, with an average pore size of 2.5 nm. This large surface area causes the creation of dangling bonds,

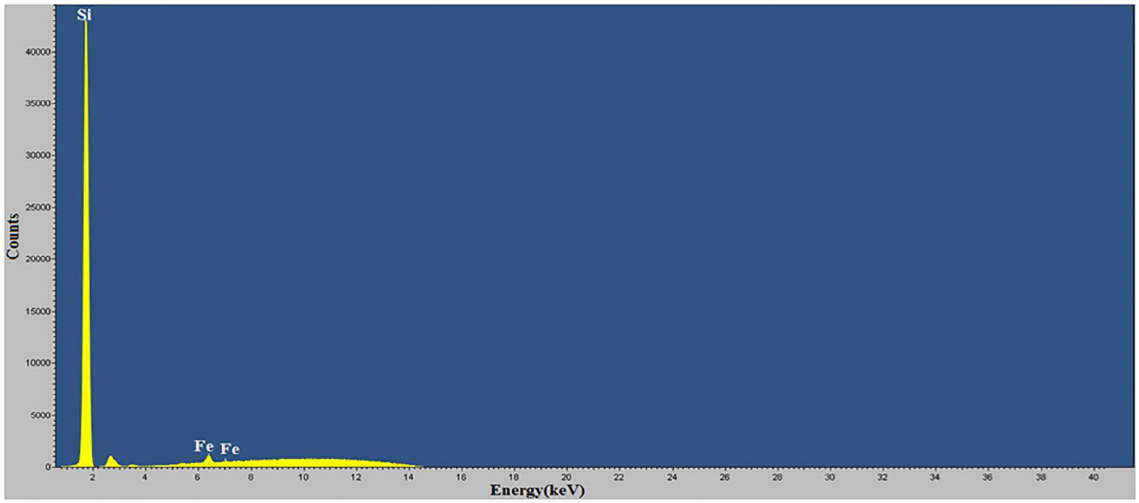

Elem.	Line	Mass[%]	3sigma	Atomic[%]	Intensity[cps/mA]
14Si	K	98.65	0.04	99.31	14990.64
26Fe	K	1.35	0.04	0.69	429.96

Fig. 1. Measured X-ray fluorescence of amorphous porous silicon nanoparticles.

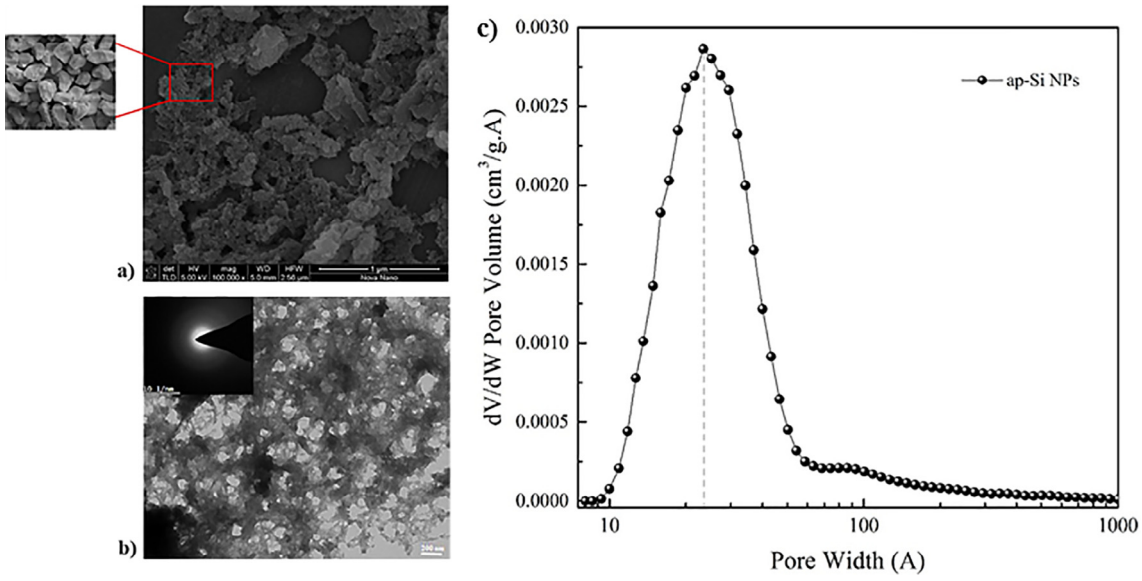

Fig. 2. (a) SEM micrograph of ap-Si NPs. A higher magnification image is shown in the inset. (b) TEM image of an array of ap-Si NPs. The corresponding SAED pattern in the inset demonstrates the amorphous structure of our NPs. (c) The pore volume vs. pore width spectrum of ap-Si NPs indicates a small mesoporous structure.

which may be the driving force behind the crystalline-to-amorphous phase transition during the etching process. The phase-transition is also confirmed by the absence of well-defined diffraction rings in the SAED pattern inset of Fig. 2b of the synthesized ap-Si NPs.

However, the formation of NPs is a very complex process. It involves nucleation, growth, coagulation, and flocculation, all of which are influenced significantly by the addition of ILs. They play an alternative solution to avoid the aggregation phenomena due to their surfactant-like structure. Nonetheless, further analysis of dispersion of NPs in ILs is needed to provide a better fundamental understanding of the dispersion mechanism. This is essential to support emerging applications of ILs in NPs synthesis, chemical reactions involving NPs, and in hybrid materials that incorporate ILs and NPs.

The effect of ILs on the morphology of ap-Si NPs in ILs are depicted Fig. 3. A well-dispersion of ~100 nm ap-Si NPs was observed within the whole bmim-SCN matrix Fig. 3b. The TEM micrograph of the ap-Si NPs in emim-BF4 also showed a good dispersion of NPs within the IL along with some aggregation into larger blobs Fig. 3c. Further analysis showed a distinct surface layer of the IL (emim-BF_4) surrounding the ap-Si NPs. However, in the case of bmim-Ac, large aggregates and stacks of ap-Si NPs were observed all over the IL matrix Fig. 3d.

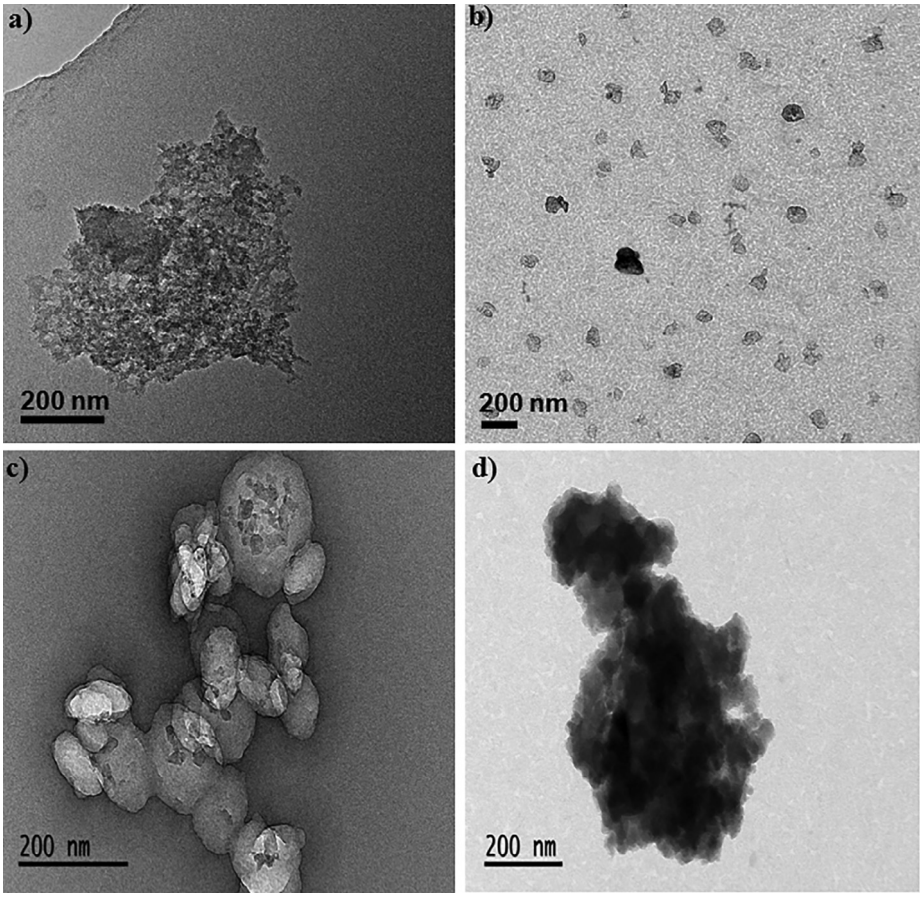

Fig. 3. HRTEM images of ap-Si NPs before and after dispersion in ionic liquids: (a) pristine ap-Si NPs, (b) ap-Si NPs/bmim-SCN, (c) ap-Si NPs/emim-BF_4, and (d) ap-Si NPs/bmim-Ac.

We used Raman spectroscopy and XRD to better understand the dispersion mechanism of ap-Si NPs in ILs, and to probe the effect of adding ap-Si NPs on the structure of the host ILs.

The spectral range of the characteristic Raman band of the three bare ILs see Fig. 4 showed various characteristic peaks associated with IL structures. The cations demonstrated strong Raman signals in the C–H stretching region in the range from 300 to 3300 cm^{-1}, where the two ILs containing $[bmim]^+$ cations exhibited a similar pattern with methyl antisymmetric vibrational modes dominating the spectrum. Based on the anion type, the anion-cation interaction is indicated by different intensities for the same vibrational mode. Every specific anion is accompanied by a frequency shift and appearance of new modes.

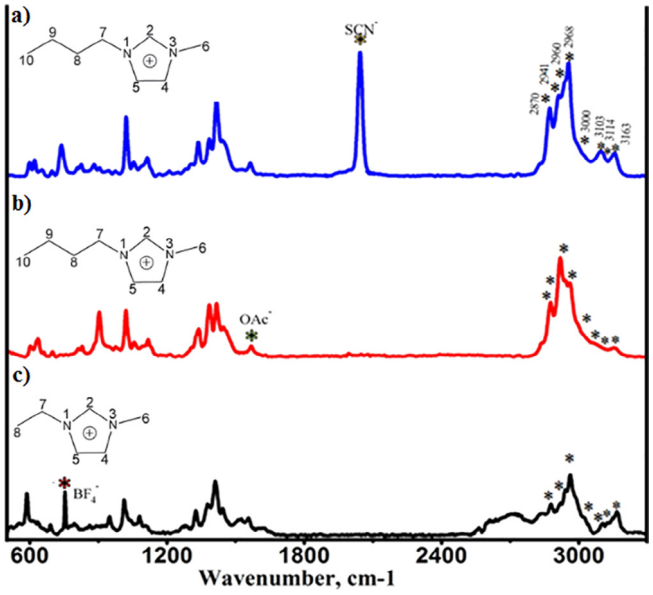

Fig. 4. Raman spectra of blank (a) bmim-SCN, (b) emim-BF_4 and (c) bmim-Ac.

A small difference in the CH_x stretch vibrational mode of $[emim]^+$ cation was observed in the range from 2800 cm^{-1} to 3300 cm^{-1}, indicating the presence of weaker bonds compared to $[bmim]^+$. This is attributed to the only one methylene group present in the ethyl ligand of the $[emim]^+$ cation rather than three methylene groups present in the butyl chain of the $[bmim]^+$ cation.

The pure bmim-SCN salt displayed five strong C–H overlapped peaks between 2700 cm^{-1} and 3200 cm^{-1}. The peaks at 2870 cm^{-1} and 2968 cm^{-1} can be assigned to the CH_3 symmetric and antisymmetric modes. The CH_2 antisymmetric vibration at 2913 cm^{-1}, the CH_3 (symmetric) Fermi resonance at 2941 cm^{-1} and the band pointing at 2960 cm^{-1}, are due to CH_3 antisymmetric modes. The peaks at 3103 cm^{-1} and 3163 cm^{-1} are for antisymmetric and symmetric stretch vibrational modes of HC(4)-C(5)H of bmim-SCN, while the peak shown at 3114 cm^{-1} is assigned to the stretch vibrational mode of C(2)-H. The N-CH_3 stretching vibration is at 3000 cm^{-1}. The Raman scattering signal at 2041 cm^{-1} for thiocyanate (SCN^-) is relative to the symmetric vibrational mode of the anion [24].

The Raman spectrum of bmim-Ac shown in Fig. 4b has almost the same peak positions except the ones corresponding to the

anion. The peaks centered at 1582.4 cm^{-1} can be associated with the stretching frequencies of C═O. In contrast, weaker bands around ~2940–2990 cm^{-1} were observed for the $[emim]^+$ and are assigned to the CH_x stretching of the ethyl chain and methyl group. In Fig. 4c strong Raman signals is observed at 754 cm^{-1} and 1121 cm^{-1} corresponding to stretching vibration of the B-F bonds in BF_4, related to the structure of the anion [24].

Fig. 5 shows a comparison between the Raman spectra of blank ILs and ap-Si NPs/ILs nanocomposites. The presence of the characteristic vibrations of ILs in the ap-Si NPs/ILs nanocomposites indicated that ILs' structures were not damaged during the irradiation process. The dispersion of ap-Si NPs in bmim-SCN did not induce any significant change in the positions of the characteristic peaks of $[bmim]^+$ compared to blank imidazolium moiety, suggesting that the incorporation of ap-Si NPs did not change the chemical structures of $bmim^+$. However, the characteristic peak of SCN anion observed at 2050 cm^{-1} in blank IL (bmim-SCN) was shifted to 2087 cm^{-1} as a result of the addition of ap-Si NPs Fig. 5a. This shift was attributed to a complexation between the thiocyanate ions and the traces of iron (Fe) impurities present in the stain etched ap-Si NPs as evidenced by the XRF. The obtained reddish dispersion of ap-Si NPs in bmim-SCN see inset of Fig. 5a confirmed this attribution. (Note that thiocyanate used to be known as rhodamine because of the red color of its complexes with iron [25,26].) This finding indicated a strong interaction between the anionic part of the IL (emim-SCN) and ap-Si NPs yielding a new adduct between the Fe(III) in the center of the complex and the thiocyanate ions $\{(Fe[SCN]_6)^{3-}\}$.

The Raman spectrum of emim-BF_4/ap Si NPs composite, shown in Fig. 5e indicated the dual contribution from both ap-Si NPs and IL. The characteristic bands of $[emim]^+$ were shifted compared to those observed in the spectrum of blank emim-BF_4. While remarkable and prominent shifts in the B-F band toward higher wave numbers were observed. In particular, a 12 cm^{-1} red shift in the BF_4^- symmetric stretching mode was experienced for the nanocomposite with respect to the band frequency of the pristine emim-BF_4. This could be an indication of the established interaction between the substrate and the probe molecule. These changes are probably due to the action of imidazolium ring and the anionic part; both of them experience a different environment in the mixture as compared to that in blank IL.

An explanation for the observed shifts is that the emim-BF4 structure had to hinge their order after dispersing the NPs, which in return provided sufficient energy to stabilize the ap-Si NPs. It is well known that ILs with the general formula emim-X or bmim-X ($X = BF_4^-$, PF_6^-, $N(CN)_2^-$, Tf_2N^-) provide stabilization to a wide range of NPs [27,28]. Thus in the case of emim-BF4, the imidazolium rings are linked by hydrogen bonding with the fluoride atoms in BF_4^-. Thereby, the addition of ap-Si NPs resulted in the reduction of the interactions between $[emim]^+$ and $[BF_4]^-$ leading to an increase in the free ions concentration inducing a red shift of the anion and cation Raman spectral bands.

In contrast, the Raman spectrum of dispersed ap-Si NPs in bmim-Ac Fig. 5c. Did not show any changes in Raman peaks' positions or intensities. The high viscosity of bmim-Ac restrained the dispersion of ap-Si NPs which prevented further experimental investigation for their performance.

XRD characterization was used to investigate the dispersion characteristics of solution-blended nanocomposites see Fig. 6.

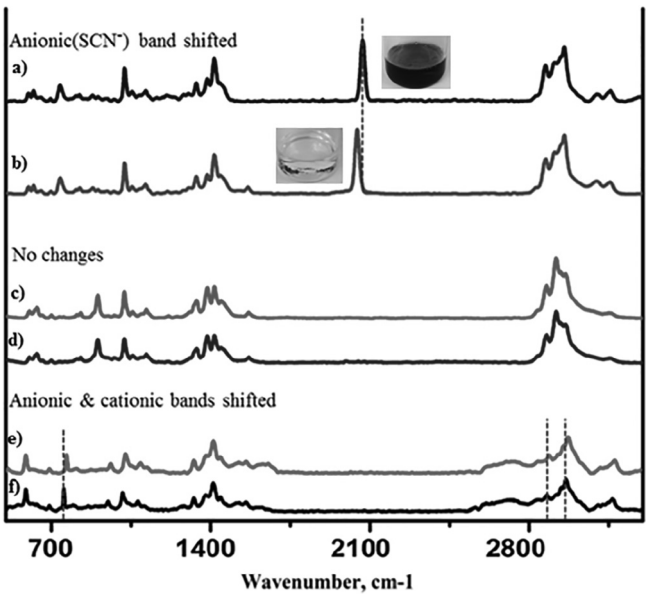

Fig. 5. Raman spectra of (a) bmim-SCN/ap-Si NPs mixture, (b) blank bmim-SCN, (c) bmim-Ac/ap-Si NPs mixture, (d) blank bmim-Ac, (e) emim-BF_4/ap-Si NPs mixture, and (f) blank emim-BF_4. Notice the induced red color as a result of adding ap-Si NPs to bmim-SCN. (For interpretation of the references to color in this figure legend, the reader is referred to the web version of this article.)

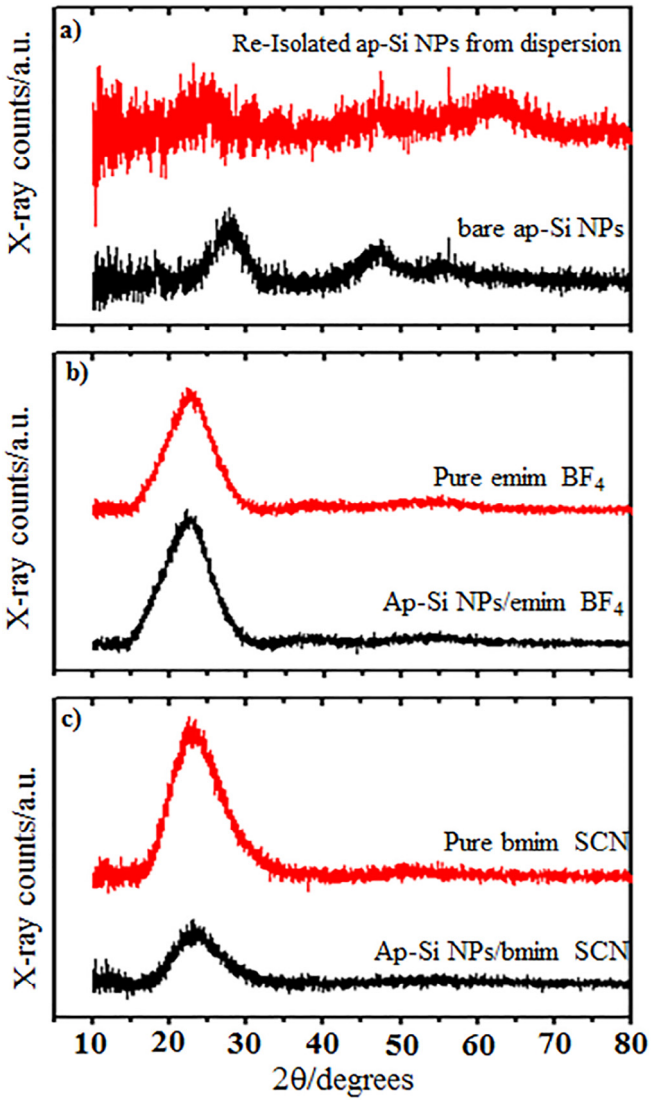

Fig. 6. XRD pattern of (a) neat ap-Si NPs and ap-Si NPs re-isolated from ILs, (b) blank emim-BF_4 and ap-Si NPs in emim-BF_4, and (c) blank bmim-SCN and ap-Si NPs in bmim-SCN.

X-ray patterns of neat NPs confirmed the amorphous structure of ap-Si NPs and exhibited intense reflexion between 20° and 30° 2θ with the most intense reflexion (1 1 1) at 28°.

X-ray patterns of neat NPs compared to the NPs isolated from ionic liquids after dispersion see Fig. 6a. Suggest that neither the structure nor the sizes changed after the dispersion of ap-Si NPs in the ionic liquids. Fig. 6b and c exhibited a single broad diffraction peak between 20° and 40° 2θ. This is not unprecedented and can easily be assigned to the liquid-like structure of the ionic liquids. There was no significant shift in the diffraction peaks that could be assigned to the dispersed ap-Si NPs Fig. 6c showed that the ap-Si NPs were highly distributed in the bmim-SCN; one can notice that from the observed positive enhancing effect as a of the presence of ap-Si NPs. This enhancement implies that, owing to the ap-Si NPs, the composite sample has more ordered arrangement than the bare IL. This result indicates that the introduction of thiocyanate can effectively promote stability of ap-Si NPs. As mentioned above, thiocyanate has a tendency to form a complex with Fe impurity [29,30], thus preventing contact with ap-Si NPs, and thereby suppressing their aggregation. Dispersion in bmim-SCN

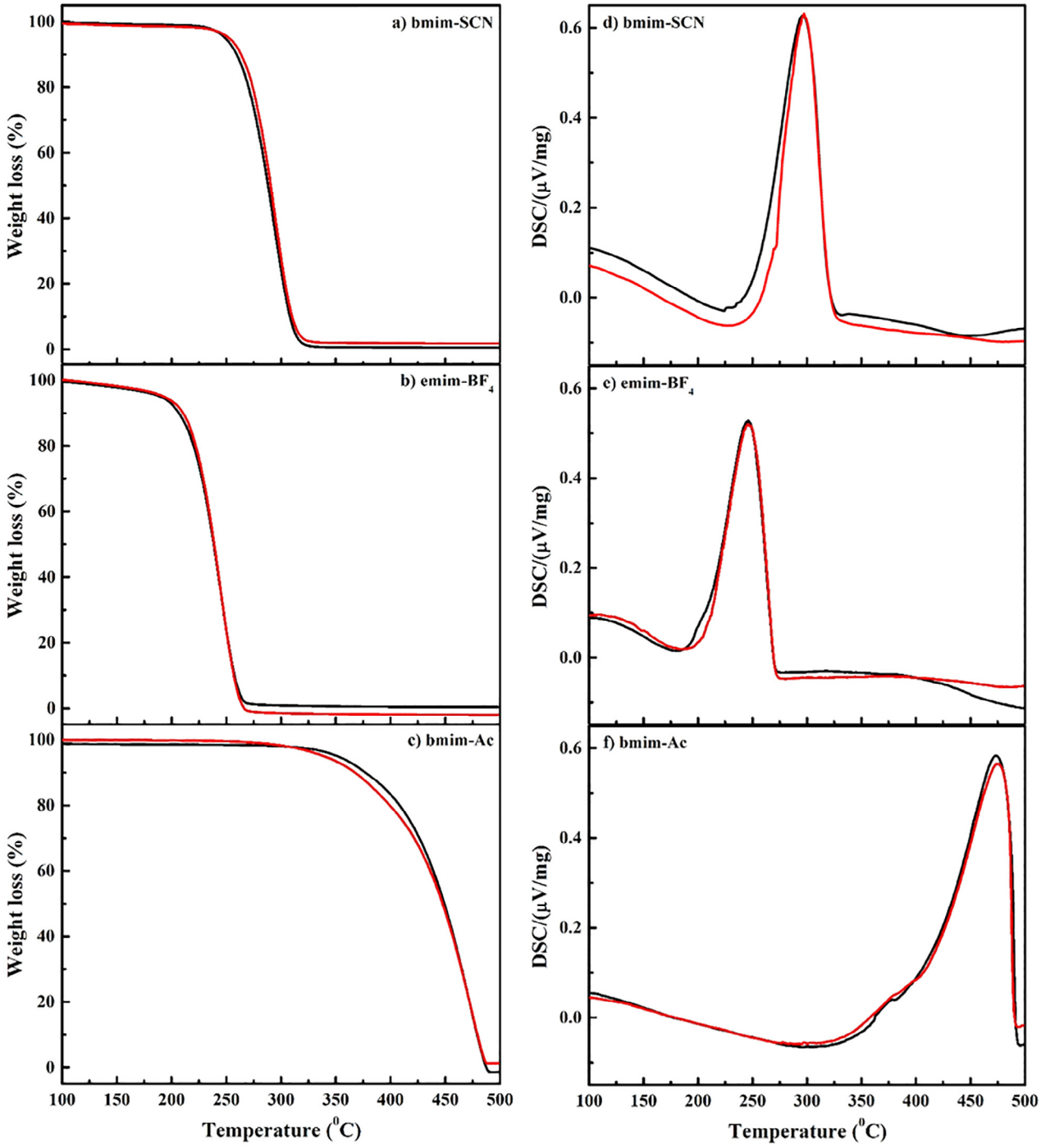

Fig. 7. Thermogravimetric analysis (TGA) (left) and differential scanning calorimetry (DSC) (right) measurements of ILs w/wo (black/red) ap-Si NPs. (a) & (d) are for bmim-SCN, (b) & (e) are for bmim-BF_4, and (c) & (f) are for bmim-Ac. (For interpretation of the references to color in this figure legend, the reader is referred to the web version of this article.)

can be seen as a quick efficient purification method for ap-Si NPs from iron impurity. This attribution is in good agreement with TEM images Fig. 3.

For nanocomposites prepared in emim-BF_4, a less degree of enhancement was found compared to those prepared in bmim-SCN, which can be attributed to the fact that the order is less. However, owing to the known intrinsic high electronic affinity between fluorine and silicon, and in addition to the steric bulk structure of ILs, it is suggested that emim-BF_4 can create an electrostatic and steric stabilization of ap-Si NPs [27,28], The strong affinity and attraction between fluorine to silicon stabilized the ap-Si NPs during the dispersion process. This would explain the role played by the thick layer surrounding the ap-Si NPs Fig. 3c.

The thermal stability of the ILs-based nanocomposites is the most important parameter for their processing applications. Thus it was very instructive to further characterize their thermal degradation behavior. The effect of incorporating ap-Si NPs on the thermal stability of ILs was investigated using thermogravimetric analysis (TGA) and differential scanning calorimetry (DSC).

The TGA and DSC measurements of the blank bmim-SCN before and after adding ap-Si NPs are shown in Fig. 7a and d. In case of blank bmim-SCN, a single-step weight loss was observed from the TGA curve starting from 250 to 325 °C. However, shifted weight loss was observed when ap-Si NPs were mixed with bmim-SCN. The weight loss observed at higher temperatures (∼15 °C) could be attributed to the strong chemical interaction between SCN and iron impurity present in the vicinity of NPs. The complexation between iron and thiocyanate was beneficial in improving the thermal stability of ionic liquids as can be seen in Fig. 7a. It is obvious that ap-Si NPs became well dispersed in bmim-SCN medium. The TGA results were supported by the corresponding DSC thermogram showing a single endothermic peak at 295 °C (IL) that was shifted to 309.5 °C after the adding the ap-Si NPs. This clearly indicated that the addition of ap-Si NPs to bmim-SCN promoted transition to a more stable phase.

In contrast to bmim-SCN, emim-BF_4 coupled with ap-Si NPs did not show such a chemical interaction. TGA and DSC results Fig. 7b and e showed that the bare emim-BF_4 was rather stabilized by physical adsorption of ap-Si NPs into the matrix. The TGA and DSC spectra of emim-BF_4 containing ap-Si NPs showed a slight shifting of ∼8 °C compared to bare IL. By stabilizing the NPs, emim-BF_4 restricted their movement making the nanocomposite more compact and stable. Thus the scission of emim-BF_4 at certain temperatures are hard and the degradation temperature of the composite shifted to higher temperature. Therefore, the interfacial interactions play an important role in the degradation of ILs nanocomposite. It should be noted that in all ILs, the first stage of weight loss from room-temperature to 200 °C was attributed to the removal of moisture. Furthermore, in the case of bmim-Ac, the IL w/wo ap-Si NPs showed higher decomposition temperature as shown in Fig. 7c and f. TGA clearly indicated that there was no weight loss up to 320 °C which usually corresponds to degradation of IL but total loss is commenced at around 485 °C. Due to the viscous nature of bmim-Ac, the interaction between NPs and IL was almost negligible and it was basically overlapping all over the TGA and DSC spectra. Consequently, it was confirmed that in terms of stabilization, bmim-SCN and emim-BF_4 are the most compatible with ap-Si NPs among the three chosen ILs.

A schematic representation of the aforementioned surface complexation of SCN− to iron atoms in the vicinity of ap-Si NPs is depicted in Scheme 1. We propose that this surface complexation led to the strong red coloring and was responsible for the good dispersion of ap-Si NPs.

Furthermore, a unique adsorption structures for emim-BF4 on ap-Si NPs were also proposed (see Scheme 2). The anionic part BF_4^- interacts with the surface of ap-Si NPs forming a negatively charged layer. The Raman spectra showed that a cationic part appeared above this negatively charged layer, forming a double layer structure. However, it seemed to be far from the surface, which justified the smaller change in the imidazolium ring behavior compared to the anionic part [31–33].

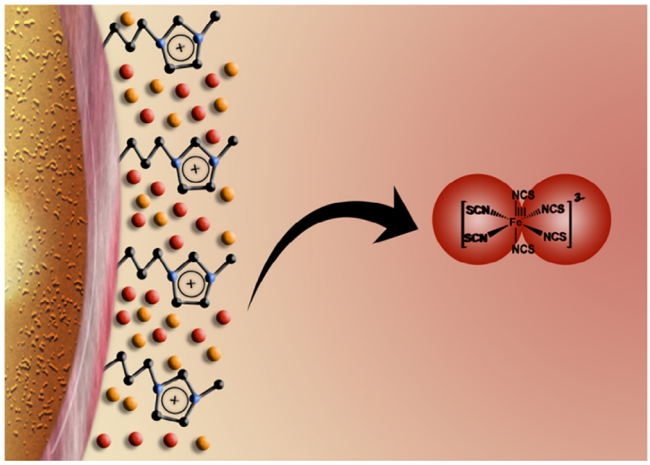

Scheme 1. A schematic illustration of iron-thiocyanate complexation $[Fe(SCN)_6]_{3-}$ in the vicinity of ap-Si NPs in the case of bmim-SCN/ap-Si NPs nanocomposites.

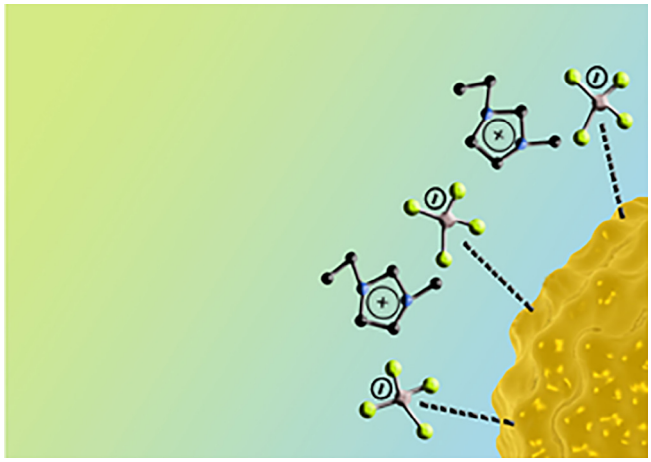

Scheme 2. Schematic representation of a structural organization of ap-Si NPS in emim-BF_4.

4. Conclusions

We studied the behavior of different dispersions of ap-Si NPs in ILs. It is well known that dispersing NPs in any solvent without capping ligands or surfactants is not a straightforward task. Nonetheless, ILs were rediscovered as alternatives to common organic solvents. They could be alternatives to such ligand layers without adding any additional stabilizers, surfactants or capping ligands, while retaining the NPs morphology. In this work, our ap-Si NPs remained intact upon dispersion as shown by the XRD analysis of the ap-Si NPs extracted from ILs.

When dispersed in the chosen ILs, the ap-Si NPs/ILs became well-organized and nanostructured in the case of some ILs, while in other cases it was difficult to study their behavior due to many limiting factors. Building upon the implications of the aforementioned experimental findings, we were able to schematically demonstrate the effect of different ILs on the dispersion quality of ap-Si NPs as well as their stability (see Scheme 3). Scheme 3

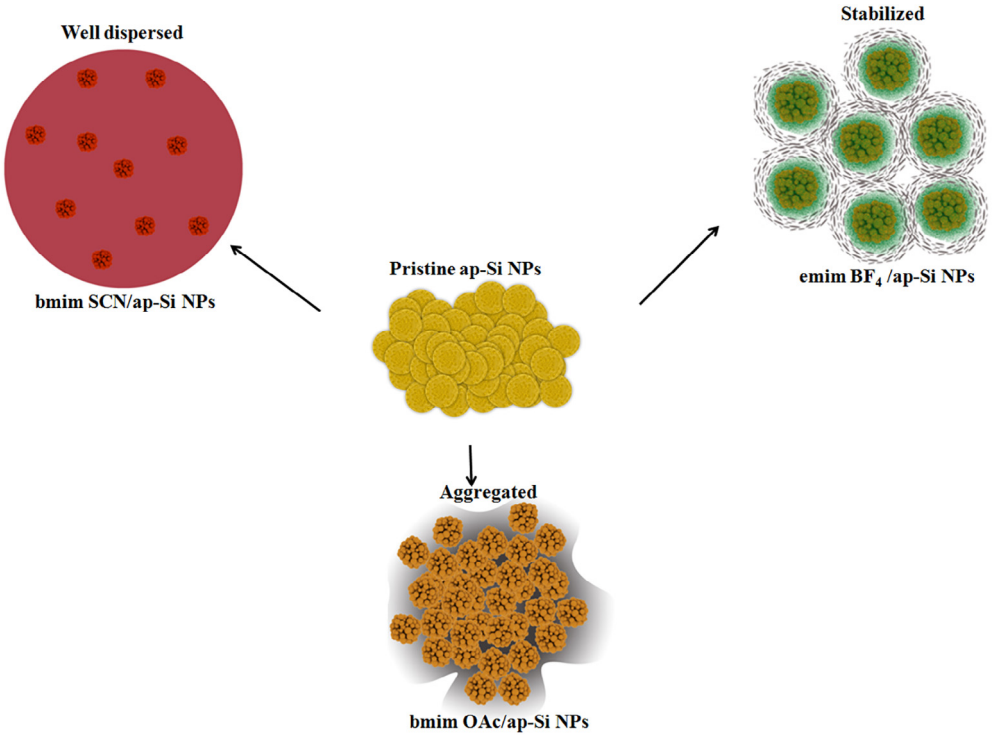

Scheme 3. A schematic representation of nonstructural dispersion of binary mixtures made of ap-Si NPs in different ILs.

illustrates how the ILs can play a determinant role in dispersion properties of NPs.

On one hand, the ap-Si NPs were able to form well-dispersion with bmim-SCN. The interaction between residual iron impurity and the anionic moiety resulted in formation of iron thiocyanate complexion inducing highly dispersed framework. While in the case of emim-BF_4, the dispersion of ap-Si NPs was affected by the contribution of electronic affinity and steric bulk behavior of the emim-BF_4. The ap-Si NPs were stabilized and the ensuing structures revealed the formation of a layer of the IL on the NPs surface via weak parallel coordination. This was attributed to an electrostatic stabilization.

On the other hand, the dispersion of ap-Si NPs in bmim-Ac induced unwanted aggregation of ap-Si NPs and did not cause any alterations, which emphasizes the fact that in case of high viscosity one should not expect any change. Thus, such ILs with relatively high viscosity are not considered as dispersants for nanostructured substances.

It is important to remark that, in addition to highlighting the dispersion quality as a result of changing the containing IL, this study provides new insights on the thermal stability of IL-based nanostructured semiconductor suspensions, particularly ap-Si NPs suspensions, highlighting a new promising field of study. Such pronounced thermal stability would expand the span of applications in which those ILs-NPs nanocomposites could be employed. Certainly, potential applications of ILs in the fabrication of electrochemical devices, such as lithium batteries, dye-Sensitized solar cells, fuel cells, supercapacitors, light-emitting electrochemical cells and field effect transistors, could be extended to the class of obtained nanocomposites formed by ap-Si NPs and ILs.

Declaration of Competing Interest

The authors declare that they have no known competing financial interests or personal relationships that could have appeared to influence the work reported in this paper.

Acknowledgement

We thank King Abdullah University of Science and Technology (KAUST) for financial support.

References

[1] Su.S. Wuac, W. Gaob, J. Lubb, F. Chunhai, J. Mater. Chem. 22 (2012) 18101.
[2] G. Nichols, S. Byard, M.J. Bloxham, J. Botteril, N.J. Dawson, A. Dennis, V. Diart, N. C. North, J.D. Sherwood, J. Pharm. Sci. 91 (2002) 2103–2109.
[3] J. Jiang, G. Oberdorster, P. Biswas, J. Nanopart. Res. 11 (2009) 77–89.
[4] M.S. Xu, D. Fujita, S. Kajiwara, T. Minowa, X.L. Li, T. Takemura, H. Iwai, N. Hanagata, Biomaterials 31 (2010) 8022–8031.
[5] S. Tsantilitis, H.K. Kammler, S.E. Pratsinis, Chem. Eng. Sci. 57 (2002) 2139–2156.
[6] K.L. Luska, A. Moores, Chem. Cat. Chem. 4 (2012) 1534–1546.
[7] L. Wang, J. Fan, Nanoscale Res. Lett. 58 (2010) 1241–1252.
[8] R.A. Sperling, W.J. Parak, Philos. Trans. R. Soc. A: Math. Phys. Eng. Sci. 368 (2010) 1333–1383.
[9] S.K. Seol, D. Kim, S. Jung, W.S. Chang, J.T. Kim, J. Nanomater. 2013 (2013) 531760–531766.
[10] H. Bönnemann, W. Brijoux, in: Active Metals, VCH, Weinheim, 1996, pp. 339–379.
[11] M. Freemantle, Chem. Eng. News 76 (1988) 32–37.
[12] P.A.Z. Suarez, S. Einloft, J.E.L. Dullius, R.F. Souza, J. Dupont, J. Chim. Phys. Phys. Chim. Biol. 95 (1998) 1626–1639.
[13] R.P. Chin, Y.R. Shen, V. Petrova-Koch, Science 270 (1995) 776–778.
[14] M.T. Clough, K. Geyer, P.A. Hunt, J. Mertes, T. Welton, Phys. Chem. Chem. Phys. 15 (2013) 20480–20495.
[15] M.R. Tchalala, J.K. El-Demellawi, E. Abou-Hamad, J.R.D. Retamal, P. Varadhan, J.-H. He, S. Chaieb, Appl. Mater. Today 9 (2017) 10–20.
[16] U. More, Z. Vaid, S. Rajput, Y. Kadam, N. Malek, J. Dispers. Sci. Technol. 38 (2017) 393–402.
[17] H. Luo, J.F. Huang, S. Dai, Sep. Sci. Technol. 43 (2008) 2473–2488.
[18] V.S.-Y. Lin, K. Motesharei, K.-P.S. Dancil, M.J. Sailor, M.R. Ghadiri, Science 278 (1997) 840–843.
[19] Y.Y. Li, F. Cunin, J.R. Link, T. Gao, R.E. Betts, S.-H. Reiver, V. Chin, S.N. Bhatia, M.J. Sailor, Science 299 (2003) 2045–2047.
[20] S. Yae, Y. Kawamoto, H. Tanaka, N. Fukumuro, H. Matsuda, Electrochem. Commun. 5 (2003) 632–636.
[21] M. Saadoun, H. Ezzaouia, B. Bessais, M.F. Boujmil, R. Bennaceur, Sol. Energy Mater. Sol. Cells 59 (1999) 377–385.
[22] A. Mughal, J.K. El-Demellawi, S. Chaieb, Phys. Chem. Chem. Phys. 16 (2014) 25273–25279.

[23] M.R. Tchalala, J.K. El-Demellawi, A.J. Mughal, S. Chaieb, J. Phys. Conf. Ser. 758 (2016) 012018–012028.
[24] C.Y. Penalber, Z. Grenoble, G.A. Baker, S. Badelli, Phys. Chem. Chem. Phys. 14 (2012) 5122–5131.
[25] E. Itabashi, Inorg. Chem. 24 (1985) 4024–4027.
[26] V. Khare, A. Kraupner, A. Mantion, A. Jelicic, A.F. Thünemann, C. Giordano, A. Taubert, Langmuir 26 (2010) 10600–10605.
[27] E. Redel, R. Thomann, C. Janiak, Inorg. Chem. 47 (2008) 14–16.
[28] S.A. Katsyuba, E.E. Zvereva, N. Yan, X. Yuan, Y. Kou, P.J. Dyson, Chem. Phys. Chem. 13 (2012) 1781–1790.
[29] A.F. Hollemann, N. Wiberg, in: W.D. Gruyter (Ed.), Lehrbuch der Anorgansischen Chemie, Berlin, NewYork, 1985, pp. 91–100.
[30] A.A. Ayi, V. Khare, P. Strauch, J. Girard, K.M.A. Taubert, Monatsh. Chem. 141 (2010) 1273–1278.
[31] R.G. Horn, D.F. Evans, B.W. Ninham, J. Phys. Chem. 92 (1988) 3531–3537.
[32] S. Perkin, T. Albrecht, J. Klein, Phys. Chem. Chem. Phys. 12 (2010) 1243–1247.
[33] S. Perkin, L. Crowhurst, H. Niedemeyer, T. Welton, A.M. Smith, N.N. Gosyami, Chem. Commun. (Camb.) 47 (2011) 6572–6574.